Supporting Information

Screen Printability Assessment of Water-based Composite Electrodes for Lithium-ion Battery

Nora Chelfouh[1], Ngoc Duc Trinh[2], Chloé Bois[2], Audrey Laventure[1] and Mickaël Dollé[1]

[1]Département de Chimie, Université de Montréal, 1375 Avenue Thérèse-Lavoie-Roux, Montréal, QC H2V 0B3, Canada.

[2]Institut des communications graphiques et de l'imprimabilité, 999 Avenue Émile-Journault, Montréal, QC H2M 2E2, Canada.

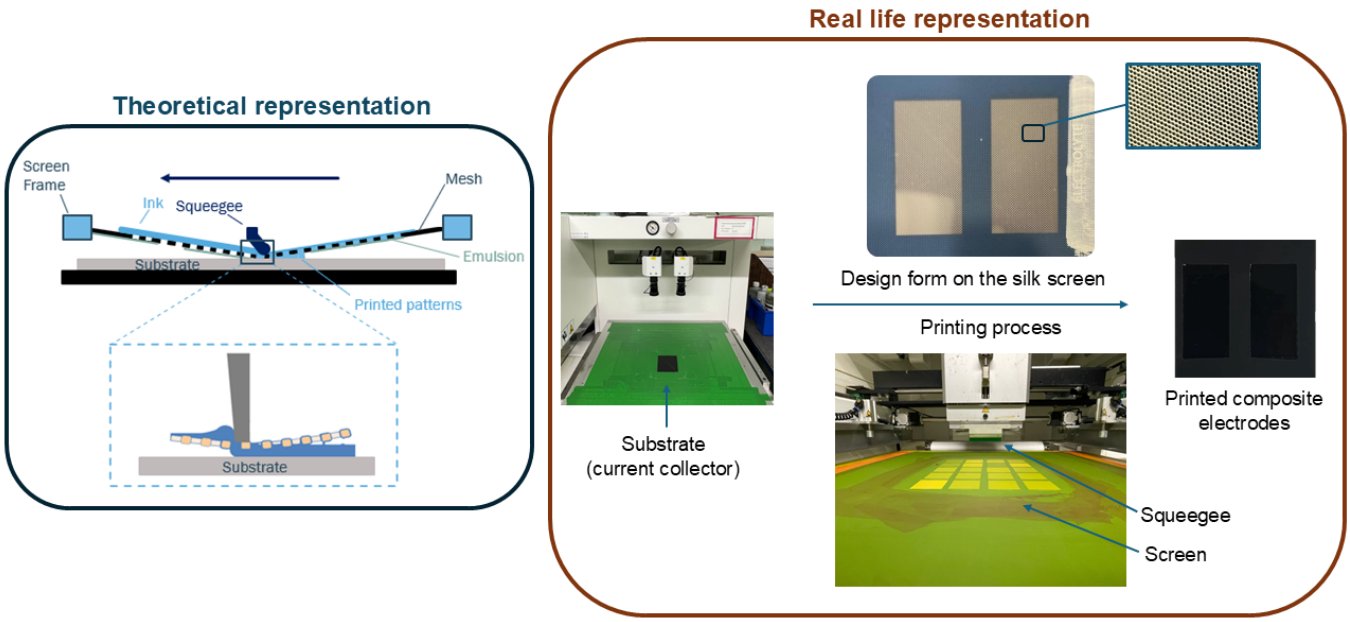

Figure S1. Flatbed screen printing process: theoretical methodology (left) vs. experimental set-up (right). The left panel illustrates the theoretical setup, including the screen frame, mesh, emulsion, squeegee, and ink deposition onto the substrate. The right panel shows real-life images of the printing setup, including the patterned silk screen, printing process, and examples of printed composite electrodes.

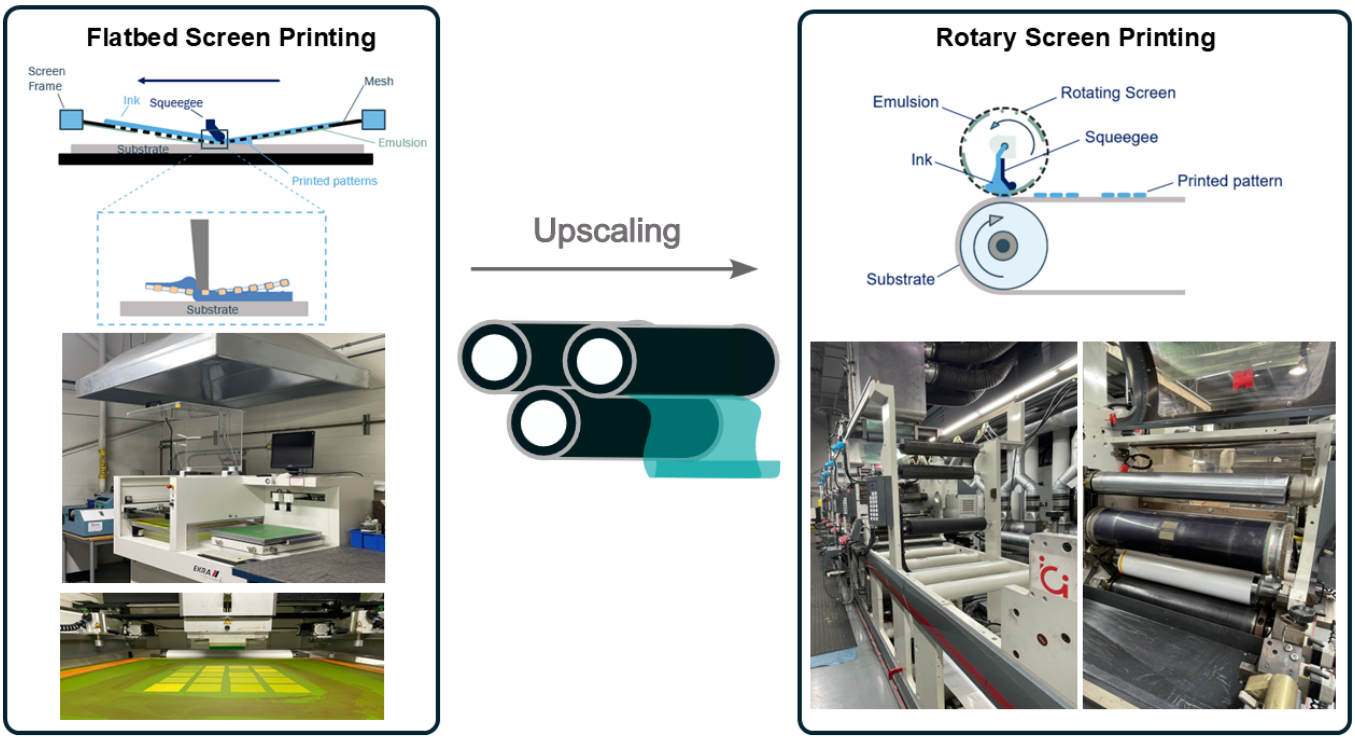

Figure S2. Upscaling process of the screen printing technique: flatbed screen printing instrument and theoretical illustration (left) to rotary screen printing process theoretical methodology and experimental set-up (right). The left panel illustrates the flatbed screen printing setup, accompanied by real-life images of the equipment in use. The right panel shows the rotary screen printing process, highlighting its continuous roll-to-roll capability.

Table S1. Composition of the slurry formulations characterized for screen-printing and rod-casting manufacturing method

	$LiFePO_4$ (wt%)	Carbon black (wt%)	CMC (wt%)	Solid content (wt%)
RC-CMC-84	83.9 ± 0.3	9.0 ± 0.1	7.1 ± 0.3	29 ± 1
RC-CMC	89.8 ± 0.1	4.9 ± 0.2	5.2 ± 0.2	32 ± 3
SP-CMC-84	83.9 ± 0.1	8.9 ± 0.1	7.1 ± 0.1	31 ± 1
SP-CMC	90.4 ± 0.1	4.5 ± 0.1	5.0 ± 0.1	36 ± 1

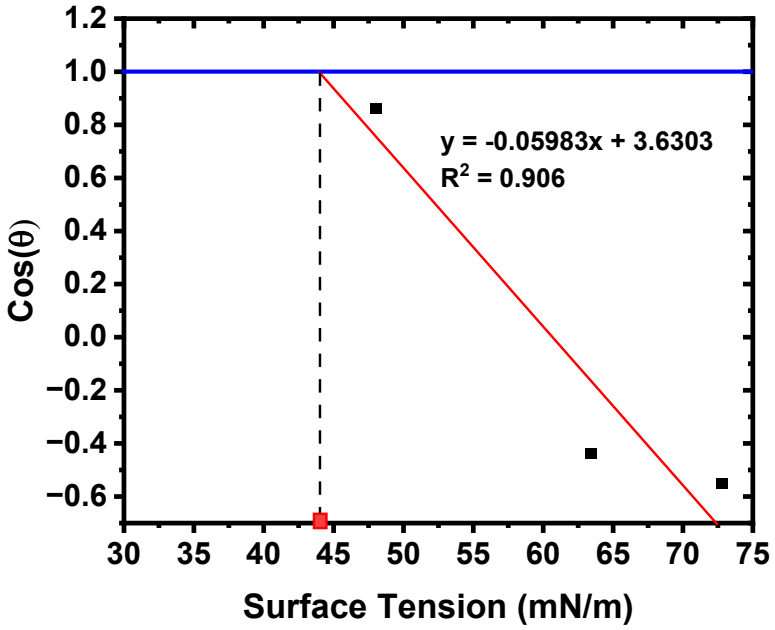

Figure S3. Zisman plot for estimating the carbon coated aluminum free surface energy

Table S2. Yield and flow point observed for RC-CMC and SP-CMC slurries

	RC-CMC	SP-CMC
Yield point (%)	1	26
Flow point (%)	60	320

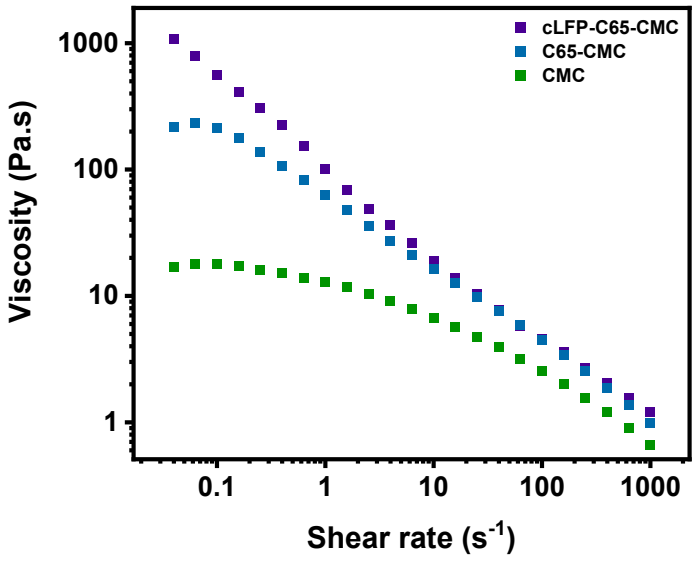

Figure S4. Flow sweep measurement for the SP-CMC slurry and its components

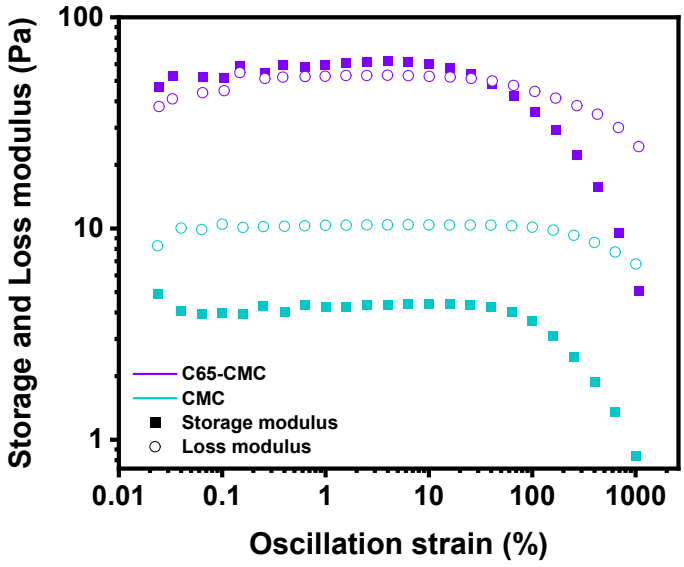

Figure S5. Storage (G') and loss (G'') moduli as a function of different oscillation strains describing the behavior of each slurry component

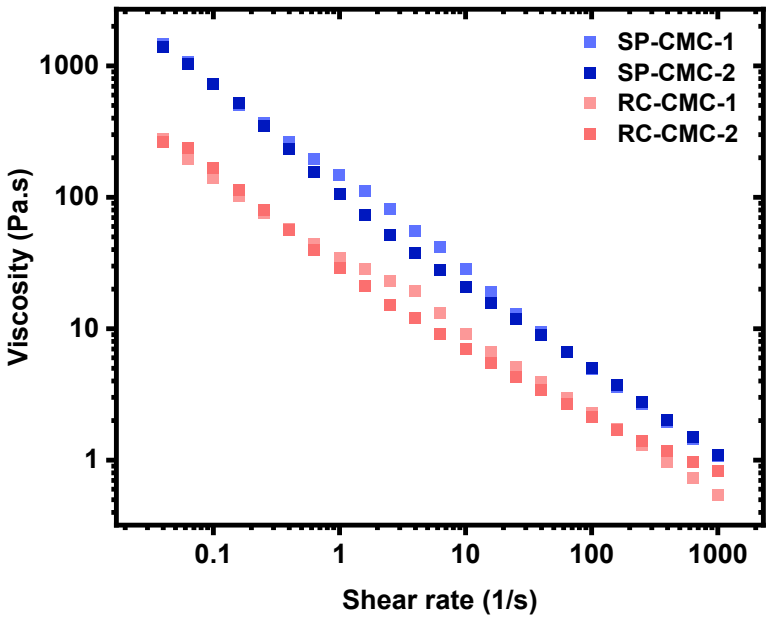

Figure S6. Flow sweep tests duplicate for the SP-CMC and RC-CMC inks.

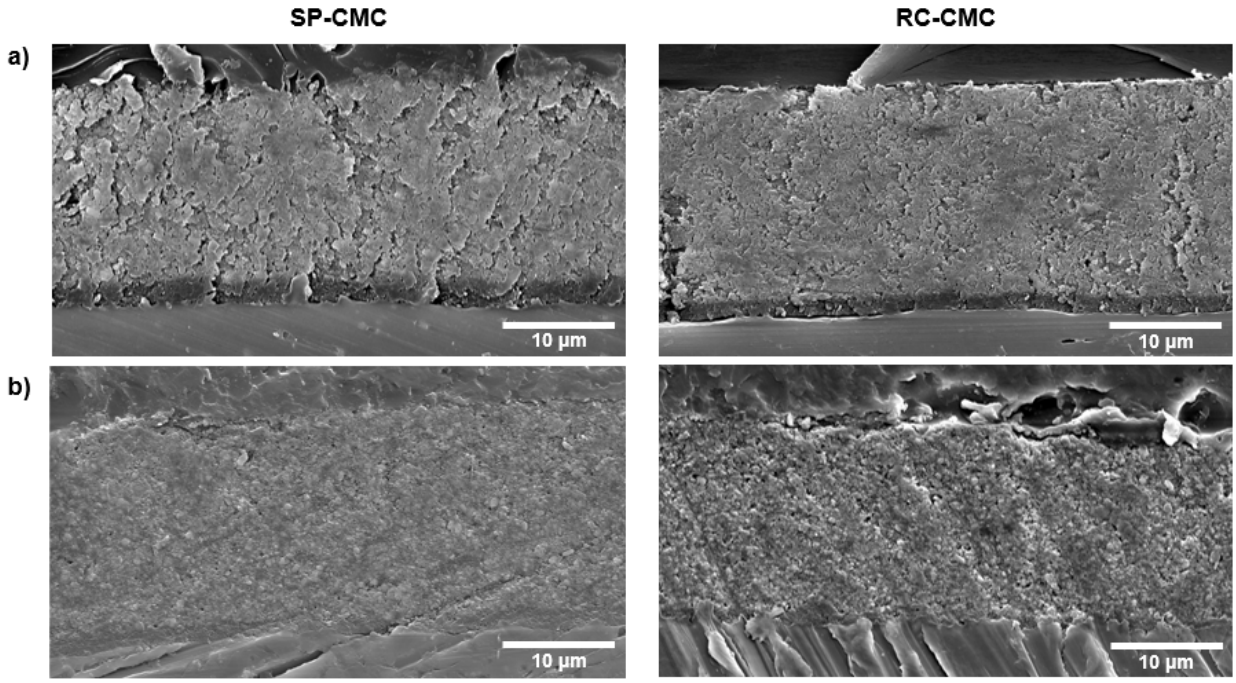

Figure S7. SEM micrographs of cross-sectional SP-CMC and RC-CMC composite electrodes before (a) and after cycling (b).

Table S3. Composite electrode thicknesses before and after calendaring, measured via micrometer.

Sample	Thickness before calendering (µm)	Thickness after calendering (µm)	Reduced thickness
RC-CMC-84	30 ± 1	23 ± 1	23 %
RC-CMC	40 ± 2	27 ± 2	33 %
SP-CMC-84	31 ± 3	23 ± 2	29 %
SP-CMC	43 ± 2	29 ± 2	33 %

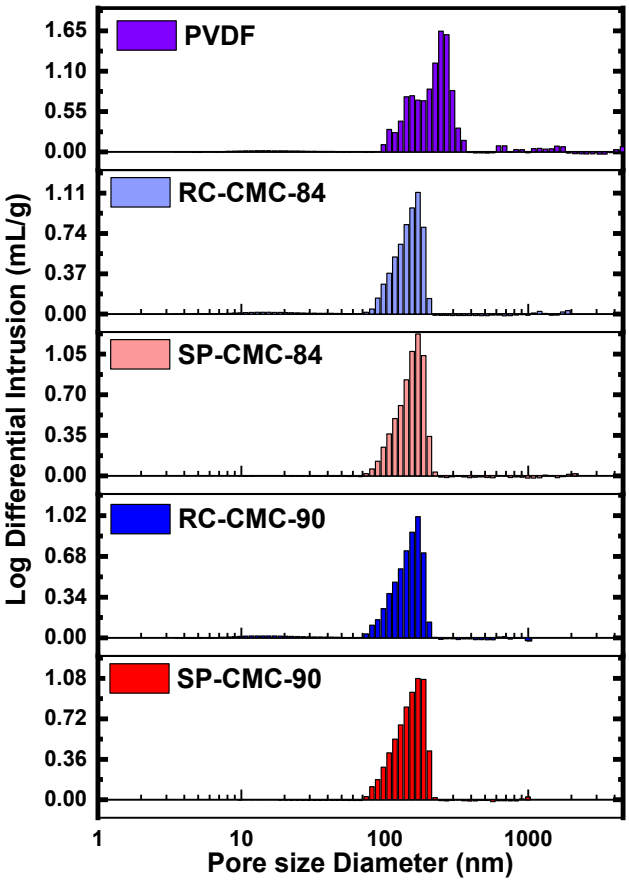

Figure S8. Pore size distributions for different printed electrodes, prepared with CMC or PVDF as a binder.

Mercury Intrusion Porosimeter

a) Instrumental parameters

The tested electrodes were cut in the shape of a (1 cm × 4 cm) rectangular stripe. The electrode was rolled in the direction of the long axis and cylinder-shaped stripe is placed in the bulb of a calibrated 5-cc penetrometer (model 09 – Micromeritics). The sealed penetrometer is then introduced in the low-pressure chamber of an AutoPore V (Micromeritics) followed by the restricted evacuation of it at a rate of 2.0 psia/min, from the atmosphere to 0.20 Torr. The evacuation then continued to 0.05 Torr with all valves of the pneumatic circuit constantly open (rapid evacuation). At that point, the penetrometer is further pumped for 5 minutes. When the penetrometer is filled with mercury (tripled distilled quality), the pressure is ≈ 0.01 Torr. Once

filled, the pressure in the pneumatic circuit is brought to 0.5 psi (25.9 Torr) and the low-pressure analysis begins. Air (99.998, bone dry, Linde) is used to intrude the mercury inside the sample. The instrument was set to record 25 points per decade between 0.5 psia to 35 psia. After each step of pressure, 10 seconds of equilibrium time is applied followed by a monitoring of the mercury rate of intrusion into the sample. The low-pressure method imposes an intrusion rate of ≤ 0.100 μL / g · s before applying the next pressure step. Once at 35 psia, the penetrometer is then introduced into the high-pressure chamber of the instrument. The high-pressure spans up to 60 000 psia and the analysis used the same intrusion method as describe above.

b) Data reduction and artifacts correction

In concordance with previous research reports, the intrusion data were calculated by considering a contact angle of 140° and by assuming the validity of the Washurn equation for the tested samples. A blank analysis, obtained with the same penetrometer and the same instrumental parameters as well, was used to blank correct the intrusion data. Samples were also corrected to consider their various levels of compressibility. The compressibility properties of the samples (linear and quadratic coefficients) are obtained by fitting the intrusion data at pressures passed the intrusion events in the sample. The two coefficients were obtained by selecting a pressure range that minimizes the root-mean-square (RMS) of the intrusion data fitting. With the computation of the linear and quadratic coefficients, it is possible to optimize the mercury intrusion pressure range to remove the low- and high-pressure artifacts. In this study, MIP analyzes were conducted on a single stripe. Therefore, the low-pressure artifact arises from the compression of the sample against the penetrometer bulb. At high-pressure values (≥ 30 000 psia) artifacts occur because of sample distortion. The linear and quadratic coefficients can ameliorate the intrusion trace at $p \geq 30\ 000$ psia. For a thin and floppy sample, the compressibility correction may not completely correct the mercury expulsion (i.e., negative intrusion), noticeable by a diminution of the intrusion signal. The lowest and the highest intrusion pressures need to be determined manually with the “Pore Structure” option available on the MicroActive software. The threshold pressure is the metric used to determine the lower pressure value. The highest pressure value of the intrusion range should give the graph of the pore diameter plotted in function the cumulative pore number % an *S*-curve. Such a curve should start à 0% and ends at 100%. The bulk and apparent densities are determined by using the optimized lower and higher pressure values respectively.

Table S4. RC-CMC and SP-CMC composite electrodes physical, chemical and electrochemical characteristics

Sample	Thickness (µm)	Loading ($mg.cm^{-2}$)	Electronic conductivity (S/m)
RC-CMC-84	23 ± 1	3.1 ± 0.2	
RC-CMC	27 ± 2	4.2 ± 0.4	9600 ± 100
SP-CMC-84	23 ± 2	3.2 ± 0.1	
SP-CMC	29 ± 2	3.9 ± 0.4	4500 ± 50

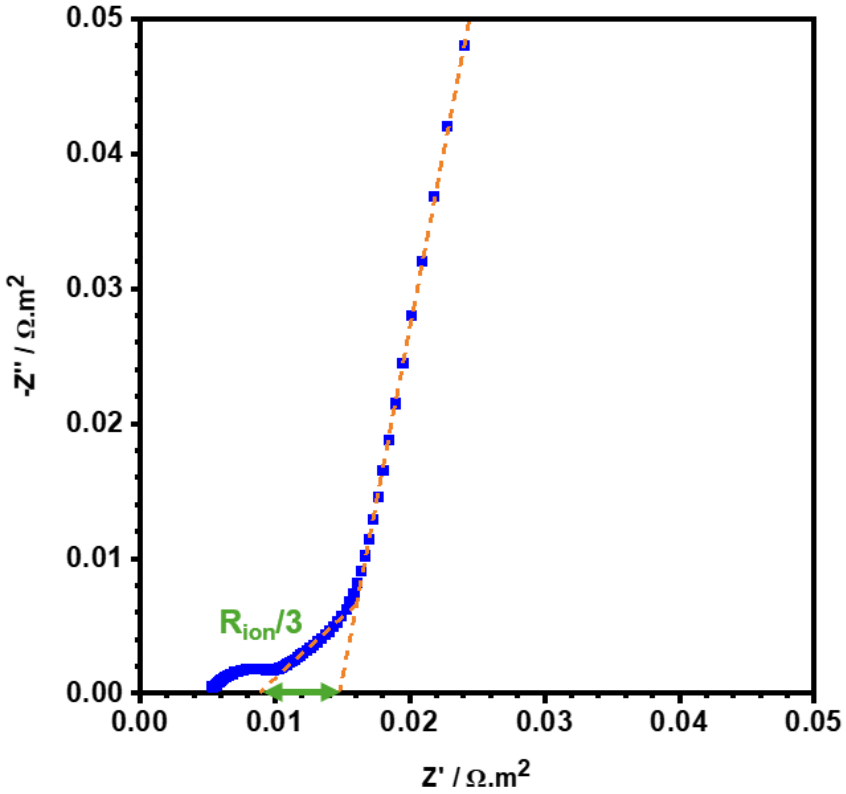

Figure S9. Experimental Nyquist plot for the SP-CMC electrode. The lines represent the extrapolation towards low and high frequencies with which the graphical method for obtaining the total ionic resistance can be extracted from, according to Landesfeind et al.

Table S5. Collected data for the tortuosity estimations

Sample	R_{ion} (ohm.m^2)	Porosity (%)	τ_{EIS}
RC-CMC-84	0.021 ± 0.004	11.6 ± 0.8	2.3 ± 0.3
RC-CMC	0.017 ± 0.003	11.6 ± 0.6	1.6 ± 0.3
SP-CMC-84	0.017 ± 0.003	15.0 ± 0.6	2.4 ± 0.3
SP-CMC	0.021 ± 0.003	12.4 ± 0.5	1.9 ± 0.2

Table S6. Detailed characteristics of each tested composite electrodes for electrochemical characterizations (cycled batteries)

Specificities	**RC-CMC**					**SP-CMC**				
Thickness (µm)	27	28	29	25	27	33	27	29	28	27
Loading (mg/cm^2)	3.58	3.44	3.58	3.64	3.70	3.78	3.97	3.91	3.95	4.07

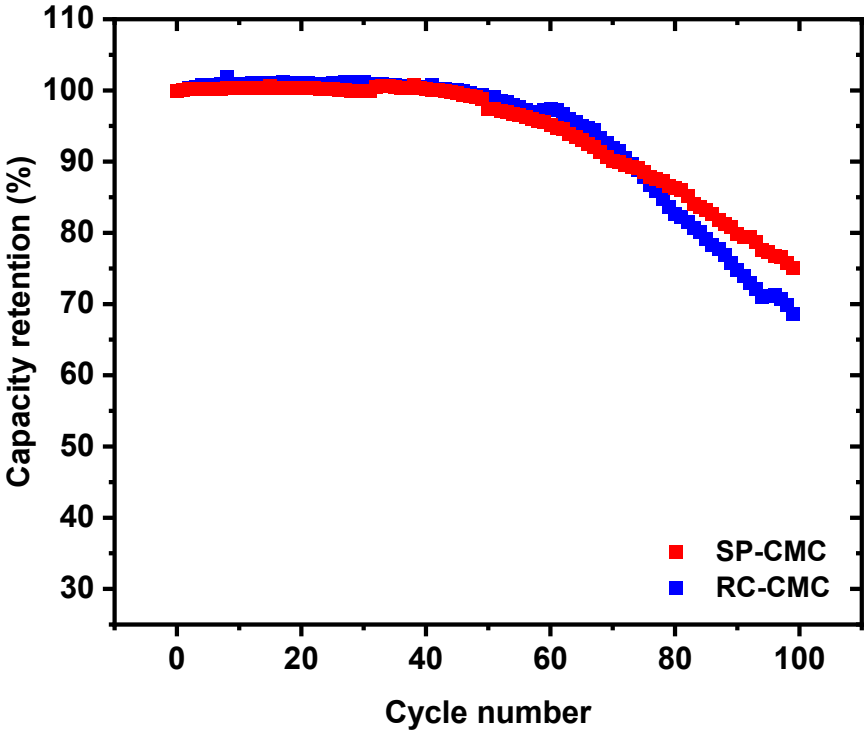

Figure S10. Life cycle of the SP-CMC and RC-CMC half cells (Li metal – negative electrode, kept for 100 cycles), at C/10